Physics of the Earth and Planetary Interiors 276 (2018) 247–257

Contents lists available at ScienceDirect

Physics of the Earth and Planetary Interiors

journal homepage: www.elsevier.com/locate/pepi

Support for equatorial anisotropy of Earth's inner-inner core from seismic interferometry at low latitudes

Tao Wang [a,*], Xiaodong Song [b,*]

[a] Institute of Geophysics and Geodynamics, School of Earth Sciences and Engineering, Nanjing University, Nanjing 210023, China
[b] Department of Geology, University of Illinois at Urbana-Champaign, IL 61801, USA

ARTICLE INFO

Article history:
Received 23 January 2017
Received in revised form 27 February 2017
Accepted 15 March 2017
Available online 20 March 2017

ABSTRACT

Anisotropy of Earth's inner core provides a key role to understand its evolution and the Earth's magnetic field. Recently, using autocorrelations from earthquake's coda, we found an equatorial anisotropy of the inner-inner core (IIC), in apparent contrast to the polar anisotropy of the outer-inner core (OIC). To reduce the influence of the polar anisotropy and reduce possible contaminations from the large Fresnel zone of the $PKIKP^2$ and $PKIIKP^2$ phases at low frequencies, we processed coda noise of large earthquakes (10,000–40,000 s after magnitude ≥7.0) from stations at low latitudes (within ±35°) during 1990–2013. Using a number of improved procedures of both autocorrelation and cross-correlation, we extracted 52 array-stacked high-quality empirical Green's functions (EGFs), an increase of over 60% from our previous study. The high-quality data allow us to measure the relative arrival times by automatic waveform cross correlation. The results show large variation (~10.9 s) in the differential times between the $PKIKP^2$ and $PKIIKP^2$ phases. The estimated influence of the Fresnel zone is insignificant (<1.1 s), compared to the observed data variation and measurement uncertainty. The observed time residuals match very well previous IIC model with a quasi-equatorial fast axis (near Central America and the Southeast Asia) and the spatial pattern from the low-latitude measurements is similar to the previous global dataset, including the fast axis and two low-velocity open rings, thus providing further support for the equatorial anisotropy model of the IIC. Speculations for the shift of the fast axis between the OIC and the IIC include: change of deformation regimes during the inner core history, change of geomagnetic field, and a proto-inner core.

1. Introduction

The inner core gradually formed and grew with the solidification of the liquid outer core, as a result of the Earth's cooling. During the solidification, latent heat and chemical differentiation (e.g., light elements are likely concentrated in the liquid outer core) provide driving energy for the geodynamo (Labrosse and Macouin, 2003; Cottaar and Buffett, 2012). Therefore, it is meaningful to explore seismic structure of the inner core to understand the evolution process and the magnetic field of our planet.

Seismic anisotropy of the inner core, casting light on its formation and dynamics (Deguen and Cardin, 2009; Alboussiere et al., 2010) and being a crucial element to estimate the rate of the super-rotation (Song and Richards, 1996), has been extensively studied last decades. It is generally agreed that the anisotropic pattern of the inner core varies with depth (Fig. 1): 1), At the topmost (~100 km), it is nearly isotropic (<1%) (Shearer, 1994; Song and Helmberger, 1995a). 2), In the outer-inner core (OIC: from 100 km to 600–700 km below the inner core boundary), the anisotropy has a symmetric fast axis aligned approximately with the Earth's north-south spin axis (Morelli et al., 1986; Woodhouse et al., 1986; Creager, 1992; Tromp, 1993; Song, 1997). In addition, distinct hemispherical structure was observed: several times weaker anisotropy in quasi-eastern hemisphere (40°E–160°E) than in quasi-western hemisphere (other longitudes) (Tanaka and Hamaguchi, 1997; Niu and Wen, 2001; Sun and Song, 2008; Irving and Deuss, 2011). 3), In the inner-inner core (IIC: about half radius of the inner core), the anisotropy shows a distinct pattern. The velocity has a minimum at an angle of ~45° from the equatorial plane in the IIC, compared with little changes for 0°–45° in the OIC (Beghein and Trampert, 2003; Sun and Song, 2008; Ishii and Dziewonski, 2002; Cormier and Stroujkova, 2005; Cao and Romanowicz, 2007). In addition, the seismic attenuation decreases with increasing depth into the inner core (Song and Helmberger, 1995b; Li and Cormier, 2002) with especially lower attenuation within the radius of about 600 km (Li and Cormier, 2002).

However, the anisotropic structures in the IIC are more ambiguous and controversial than in the OIC, due to the limitations of

* Corresponding authors.
E-mail addresses: twang0630@nju.edu.cn (T. Wang), xiao.d.song@gmail.com (X. Song).

http://dx.doi.org/10.1016/j.pepi.2017.03.004
0031-9201/

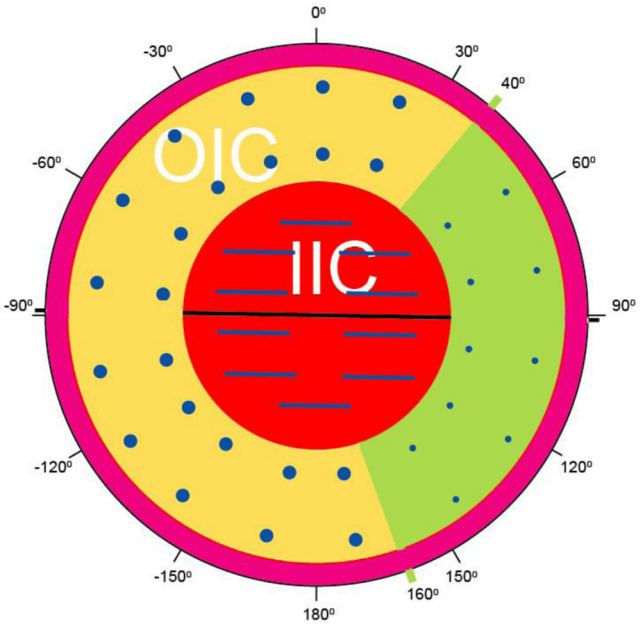

Fig. 1. A schematic model for the anisotropy of the inner core in the polar view. Three layers are shown: the uppermost isotropic layer (purple), the OIC (green: quasi-eastern hemisphere, yellow: quasi-western hemisphere) and the IIC (red). In the OIC, blue solid circles represent the N-S fast axis and the radius denotes the strength of the anisotropy. In the IIC, the fast axis (the black line) and anisotropic equatorial fast directions (blue lines) are shown. (For interpretation of the references to colour in this figure legend, the reader is referred to the web version of this article.)

traditional seismic data (normal modes and PKP waves). Normal-mode data lose sensitivity to the central inner core (Ishii et al., 2002). For PKP waves, data at large distances (>∼164°) between the earthquake and station are required to sample the IIC (radius: ∼600 km). Absolute travel-time of the PKP(DF) (also called PKIKP), corrected by tomographic models, depends heavily on the accuracy of the models in the crust and mantle. It is also affected by earthquake mislocation. To eliminate the contamination from the crust and mantle, the differential time between PKP(DF) and PKP(AB) is often used since their raypaths are close in most of the mantle. But, at large distances, the differential time is strongly influenced by the structure near the core mantle boundary (CMB) (Song and Helmberger, 1997; Brëger et al., 2000). Because the piercing points of the two phases at the CMB are well separated (e.g., by ∼37.4° at the epicentral distance of 164° and greater at larger distances). The PKIIKP is a better choice as the reference phase since its piercing point at the CMB only varies ∼10° with the PKP(DF) (Niu and Chen, 2008). On the other hand, due to the weak reflection at the underside of the inner core boundary (ICB), the available PKIIKP is very rare -- only two earthquake-array pairs found by Niu and Chen (2008). It seriously hinders the usefulness of this reference phase.

Seismic interferometry has been extensively used to retrieve the empirical Green's functions (EGFs) of surface waves (e.g., Shapiro et al., 2005; Zheng et al., 2008; Yao and van der Hilst, 2009). It has recently been used to retrieve body waves (e.g., Poli et al., 2012; Lin et al., 2013; Boue et al., 2013; Nishida, 2013). From autocorrelation (AC) of the earthquake coda, two core phases $PKIKP^2$ (I2) and $PKIIKP^2$ (II2) (round-trip of PKIKP and PKIIKP) were successfully retrieved (Wang et al., 2015). This new application of seismic interferometry greatly overcomes the above limitations of PKP body waves and provides an unprecedented global coverage for deciphering the anisotropy of the IIC. With 57 global station arrays (hereafter referred this global dataset as GD0), we found that the seismic anisotropy in the IIC had a fast symmetry axis aligned near the equator (at 9°, −89° or its antipode −9°, 91°) and had a different form of anisotropy from that of the OIC (Wang et al., 2015).

Subsequently, using PKIKP arrival times picked by hand, Romanowicz et al. (2016) argued that the model with quasi-equatorial fast axis of the IIC could not fit the arrival times of the phase PKIKP from earthquakes at antipodal distances (165–180°). After correcting the ballistic PKIKP dataset for different tomographic models, they compared models of the fast-axis orientation and preferred the N-S fast axis in the IIC. They questioned whether the two phases extracted by AC functions correspond to the assumed ballistic paths, especially for the II2.

In this study, we examined the validity of the near-equatorial anisotropy in the IIC from seismic interferometry. We used only stations at low latitudes (≤ ±35°), which are less sensitive to the anisotropy with the N-S fast axis. Furthermore, due to the slow change of velocity for equatorial paths from the N-S anisotropy in the OIC, the influence of large Fresnel zone at low frequencies (Fig. 2) can be reduced if only low-latitude stations are used.

In our previous study (Wang et al., 2015), most data were from 2005 to 2012. At low latitudes (≤ ±35°), we obtained 32 stacked EGFs from the ACs of 774 stations. We grouped the stations into arrays by visual inspection and visually adjusted a few travel-time picks with distorted waveforms. In this study, we systematically processed all low-latitude data from 1990 to 2013. We used a total of 1561 stations and obtained 52 stacked EGFs from both ACs and cross-correlations (CCs). The high-quality data allowed us to measure the relative arrival times by automatic waveform CC. In Section 2, we discuss a number of data selection and processing strategies that we used to enhance the data quality. In Section 3, the results show a similar pattern with the GD0 and are consistent with the equatorial IIC model proposed in our previous study (Wang et al., 2015). In Section 4, we discuss the difficulty of resolving the equatorial anisotropy of the IIC with earthquake PKIKP arrival times and possible mechanisms for explaining the large transition of the fast axis.

2. Data and method

2.1. Data selection

We systematically processed 24 years (1990.1–2013.12) of large earthquakes (magnitude ≥7.0) and coda waves at all broadband stations (BHZ component) at low latitudes (within ±35°). All the original data were downloaded from the Incorporated Research Institutions for Seismology Data Management Center (IRIS DMC). Most data were from the 8-year period (2005.1–2012.12) used in our previous study (Wang et al., 2015). Due to source heterogeneity for seismic interferometry, the EGFs may be unreliable if the average number of large events in an array is less than 8 (Wang et al., 2015). Therefore, to ensure the convergence of the EGFs, we first discarded the stations if they recorded less than 10 large earthquakes (all types with magnitude ≥7.0). Then, we used a grouping technique (Liang et al., 2004) to automatically divide stations and determine center points of arrays with a specific radius (2°). Compared with the GD0 (arrays selected by visual inspection), this grouping process was systematic and less subjective. Bootstrap tests indicated that the variation of the II2-I2 differential times significantly reduced (<1.5 s) when the number of stations was larger than 10 (Wang et al., 2015). Therefore, we only selected arrays if they contained at least 10 seismic stations. To increase the sampling density around the proposed fast axis of the IIC (Wang et al., 2015), we added three arrays in Central America (Table 1). Although they might have fewer stations

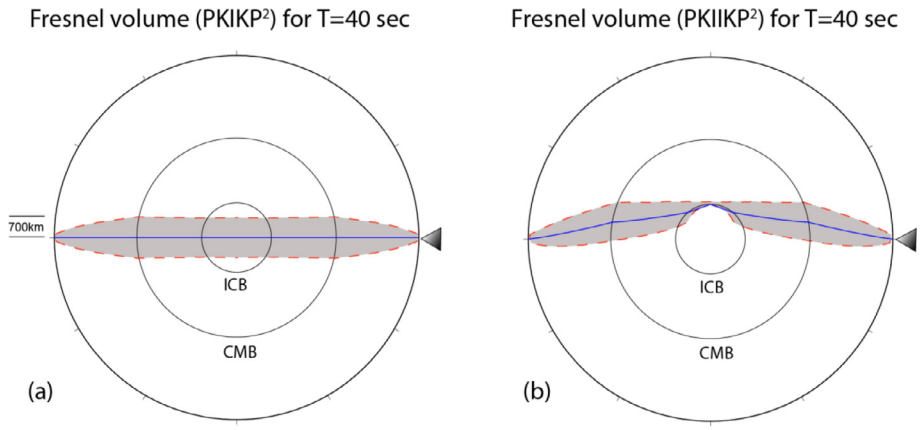

Fig. 2. Fresnel volume (grey) of PKIKP^2 (a) and PKIIKP^2 (b) at low frequency (period: 40 s). The shallowest depth of the PKIKP^2 Fresnel zone is ~700 km from the center of the inner core and the deepest region of the PKIIKP^2 Fresnel zone is ~200 km below the inner core boundary (ICB). Ray paths (blue lines) and stations (black triangles) are plotted. (For interpretation of the references to colour in this figure legend, the reader is referred to the web version of this article.)

and/or larger apertures, the waveforms and residuals in these arrays were consistent with other arrays nearby. Finally, a total of 1561 stations in 52 arrays were obtained (Fig. 3). The number of stations (*Ns*) in each array ranges from 6 to 89, with the mean of 30. We calculated the AC of a single station and the CC between a pair of stations within the array.

2.2. Improved signal processing

We modified the method for retrieving II2-I2 residuals from our previous study (Wang et al., 2015). The original data were first decimated to 0.2 s. We cut the coda (10,000–40,000 s) of large earthquakes and then band-pass filtered it between 15 and 50 s. After time domain normalization with a running-absolute-mean to reduce the effect of energetic sources and spectral whitening (Bensen et al., 2007), we calculated the AC and CC for each single-station and station pair within an array, respectively. Then, to obtain stable EGFs, we added all ACs and CCs in each array, respectively, to obtain the stacked AC and the stacked CC.

A few modifications were made in the data processing to enhance signal-to-noise ratio (SNR) of the EGFs, compared with our previous study (Wang et al., 2015), which used only ACs. First, we chose a better coda time-window (10,000–40,000 s) for the correlations, instead of 10,000–30,000 s (Wang et al., 2015), as suggested previously (Xia et al. 2016; Lin and Tsai, 2013). Here, we illustrated two typical results of the dense (the master array at 31.60 °N, 103.52 °W and *Ns* = 76) and sparse (an array in Central America at 13.80 °N, 62.00 °W and *Ns* = 6) arrays. For both arrays, the stacked ACs with the coda of 10,000–40,000 s (10k–40 k) was a better option to enhance the SNR of both I2 and II2 (Fig. 4). In particular, the improvement of this time-window in retrieving clear I2 might be significant for sparse arrays.

Second, the SNR of the AC/CC in each station/station pair was considered as a weight in the stacking process. The AC/CC was calculated for the coda of every earthquake and then added together. As a result, the amplitude of AC/CC was significantly affected by the number of recorded earthquakes at each station. To avoid the stacked EGFs being dominated by few stations with long recording history, Wang et al. (2015) normalized each AC by the maximum amplitude in the range of containing both I2 and II2 (2000–3000 s) before the array stacking. In this study, we instead normalized each trace by the standard deviation of 2000–3000 s. This approach was, to some extent, equivalent to dividing the average noise level of each trace and hence imposed the SNR as the weight in the stacking process. Our bootstrap tests of ACs in the master array showed the standard-deviation normalization could obtain more convergent EGFs (Fig. 5a) and also enhance the SNRs of stacked results (Fig. 5b). Although the improvement was small because of similar SNRs in the master array, we expected the standard deviation normalization would increase significantly the stability of the stacked EGFs if the SNRs of AC/CCs in a single array varied greatly.

Furthermore, we imposed a selection filter (Wang et al., 2015; Nakata et al., 2015) to improve the SNR of stacked waveforms for each array. We stacked all ACs or CCs first to obtained an initial stack and cross correlated each trace with the initial stack using the time window of phase I2 (2370–2440 s). We retained only the traces for which the time-lag was less than 7 s and the correlation coefficient was larger than 0.5. The threshold of the time-lag (7 s) is the same as travel time variation of the IIC prediction in Wang et al. (2015). Larger time-lag (>7 s) may be caused by unstable signal or local heterogeneity. We then stacked the retained ACs or CCs again. The selection filter can remove incoherent waveforms due to their low SNRs or local heterogeneities under stations. For the sparse array in Central America, it significantly increased the SNRs of both stacked I2 and II2 (Fig. 4). On average, we retained about 85.7% of traces with the selection filter.

2.3. Travel-Time measurements

All arrival times for the I2 and II2 were automatically measured by using cross-correlation between stacked traces and the master one. The correlation time-windows for phase I2 and II2 are 2370–2440 s and 2470–2500 s, respectively. We defined the differential-time residual as the measured II2-I2 time minus the reference value of 66.5 s, which is the average value of the differential times of the GD0. Using the same reference makes it easy to compare with the previous study of Wang et al. (2015). For comparison, the average value of the differential time of all the measurements in this study is close at 66.8 s. Since the waveforms were more coherent with above approaches, we did not manually re-picked some of the poorer traces as we did previously (the dataset GD0) (Wang et al., 2015).

3. Results

Both the I2 and II2 phases of stacked ACs and CCs from 52 arrays were retrieved by the coda interferometry (Fig. 6). Since the aperture of most arrays was small (96.2% of 2°), the waveforms and residuals of stacked ACs and CCs, especially for dense arrays, were highly similar. The standard deviation of the residual's difference between the stacked AC and CC was 0.79 s. The SNRs of the CCs

Table 1
Detailed information for all 52 arrays used in this study.[†]

Location (Lat°, Lon°)	Rad (°)	*Ns*	Residual (s)	Std (s)	Correlation type
4.01, 11.12	2.0	12	3.4	0.8	AC
−27.49, 25.85	2.0	19	2.1	0.9	AC
−23.66, 26.40	2.0	17	−2.7	0.7	AC
−0.03, 31.20	2.0	10	1.3	1.0	AC
−9.05, 33.97	2.0	17	0.3	1.1	AC
−5.30, 36.09	2.0	14	0.7	1.0	AC
8.78, 39.36	2.0	33	−1.4	0.9	AC
12.64, 39.43	2.0	16	−1.4	0.8	AC
11.32, 40.80	2.0	29	−1.2	0.6	AC
32.14, 84.64	2.0	50	−4.3	0.7	AC
28.38, 85.36	2.0	89	−0.7	0.5	AC
31.94, 90.14	2.0	58	−1.4	0.8	AC
33.74, 95.39	2.0	22	−1.5	0.9	AC
30.69, 95.55	2.0	39	−0.2	1.3	AC
34.08, 103.55	2.0	15	−0.1	0.9	AC
23.23, 121.63	2.0	30	0.0	0.6	AC
−9.64, 150.53	2.0	34	2.2	1.2	AC
−17.73, 178.82	2.0	19	1.3	1.4	AC
20.11, −155.96	2.0	22	−2.4	1.5	AC
18.66, −153.31	2.0	13	−4.8	1.2	CC
34.11, −118.10	2.0	39	0.0	0.3	AC
33.13, −116.27	2.0	69	0.0	0.3	AC
33.36, −112.39	2.0	31	−1.2	0.5	AC
33.37, −108.01	2.0	44	−0.5	0.4	AC
33.60, −104.91	2.0	74	0.4	0.3	AC
19.57, −103.64	2.0	39	−1.7	0.7	AC
31.60, −103.52 M	2.0	76	−0.6	0.3	AC
33.41, −100.29	2.0	34	1.5	0.4	AC
29.12, −98.47	2.0	38	−1.2	1.0	AC
32.05, −96.29	2.0	48	−2.7	0.6	AC
33.96, −93.22	2.0	22	0.5	0.5	AC
31.43, −91.46	2.0	17	−0.5	0.3	CC
−0.67, −90.99	2.0	29	1.6	0.6	AC
34.22, −88.40	2.0	16	1.1	0.7	AC
12.72, −86.52	2.0	31	3.3	0.6	AC
32.82, −85.47	2.0	34	0.7	0.4	AC
10.80, −85.09	2.0	45	4.8	0.6	AC
30.90, −83.23	2.0	30	1.1	0.5	AC
27.48, −81.33	2.0	17	3.7	0.7	AC
33.69, −81.08	2.0	56	3.1	0.7	AC
−15.23, −70.78	2.0	15	−3.7	1.3	AC
−31.39, −69.32	2.0	39	−1.0	0.6	AC
−16.84, −68.21	2.0	30	−3.5	0.6	AC
−26.46, −68.19	2.0	21	−1.2	1.5	AC
−27.25, −66.93	2.0	11	0.6	1.2	AC
−31.00, −65.80	2.0	23	1.1	0.7	AC
18.13, −65.40	2.0	20	3.2	1.2	CC
32.78, −4.77	2.0	26	0.8	0.5	AC
34.82, −3.83	2.0	10	0.4	0.5	AC
5.00, −77.00[CA]	6.0	7	6.1	1.2	AC
9.50, −70.00 [CA]	2.0	6	5.5	1.8	AC
13.80, −62.00 [CA]	3.0	6	4.5	1.6	AC

[†] The central position (latitude: Lat, longitude: Lon) and the radius (Rad) for each array are listed. *Ns* represents the number of stations in each array. [M]The master array is chosen for travel-time residual measurements by waveform cross-correlation. Correlation type used for each array and corresponding bootstrapping estimated standard deviation (Std) of time residual are shown. [CA]Three additional arrays in Central America contain less stations (<10).

are similar to or maybe slightly better that those of the ACs, but we preferred the stacked ACs rather than the CCs because: 1) during the stack procedure, the move-outs of CCs, which were not considered, might increase the uncertainty of the residuals. While ACs represent zero-offset results, we can stack them directly. 2) Sens-Schonfelder et al. (2015) found the energy in late coda was not equipartitioned unless the earthquake and the stations were located on a great circle. Therefore, the arrival times of retrieved CCs can be biased by the lack of energy equipartitioning. But it cannot influence the ACs because they automatically satisfy the condition of great-circle location.

On the other hand, the available number of CCs for stacking is $Ns * (Ns - 1)/2$, which is much larger than the number of ACs (Ns). We found that the stacked ACs from three arrays had large standard deviations (from bootstrapping) but the stacked CCs were relative stable (standard deviation <1.3 s) (Fig. 7). The waveforms also indicated the SNRs of I2 and II2 phases were higher for CCs than for ACs (Fig. 7). Therefore, we used the stacked ACs mostly and used the CCs only if the I2 or II2 of the stack AC was apparently inferior (i.e., for the three mentioned array). Collectively, we obtained 52 stacked EGFs from 1561 stations, including 49 ACs and 3 CCs (see Fig. 3 and Table 1), compared with 32 stacked ACs from 774 stations in GD0 at low latitudes ($\leq \pm 35°$).

The residuals from 52 arrays at low latitudes vary greatly (−4.8∼6.1 s) with a standard deviation of 2.4 s. The large variation cannot be explained by an anisotropic model with the N-S fast axis, whether it's uniform (Romanowicz et al., 2016) or more complex such as hemispherical (*e.g.*, Lythgoe et al., 2014). In addition, large variation of the residuals cannot mainly arise from local heterogeneity or errors of a few stations. Because using a bootstrapping

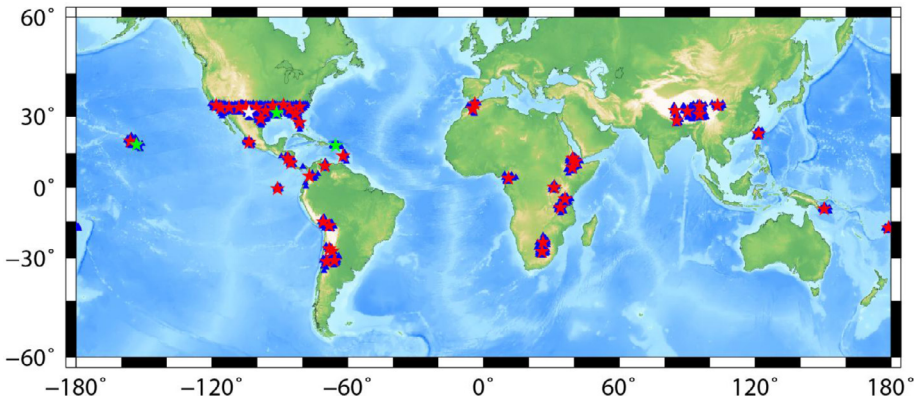

Fig. 3. Map of stations (blue triangles) and 52 arrays (stars) used in this study. Master array (white star) for automatic travel-time picking is plotted. 49 ACs (red stars) and 3 CCs (green stars) are used for retrieving the I2 and II2. (For interpretation of the references to colour in this figure legend, the reader is referred to the web version of this article.)

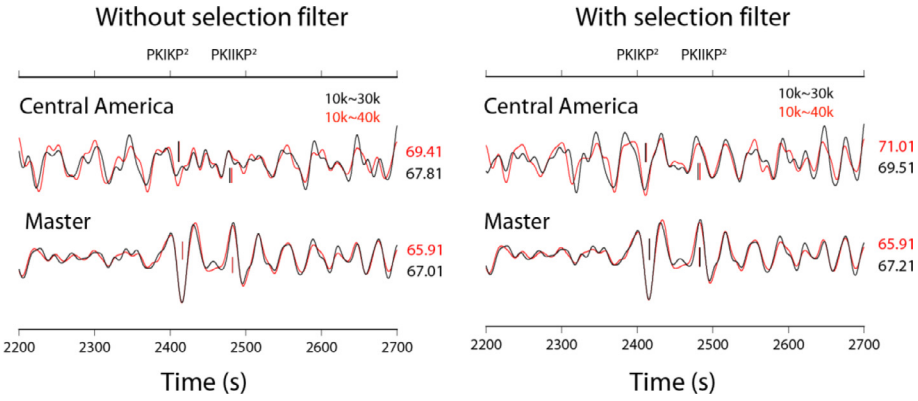

Fig. 4. To show the influence of coda window and the selection filter. Two coda windows (10 k–30 k: black, 10 k–40 k: red lines) are compared for obtaining ACs without (a) and with (b) the selection filter, respectively. Two typical arrays are tested: the master array (Lat: 31.60°N, Lon: 103.52°W, 76 stations) and the array in central America (Lat: 13.80°N, Lon: 62.00°W, 6 stations). Differential times (numbers in the right) and waveforms show it is a better choice of retrieving stable I2 and II2 phases by using the coda of 10,000–40,000 s and the selection filter, especially for the array with a small number of stations. (For interpretation of the references to colour in this figure legend, the reader is referred to the web version of this article.)

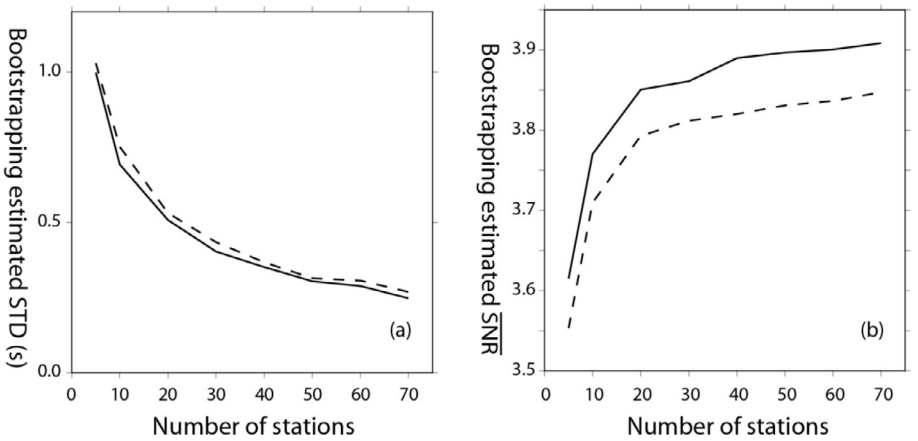

Fig. 5. Comparison of two different normalization methods before stacking for the master array. Bootstrapping-estimated standard deviations (STD) of residuals (a) and average SNRs (b) indicate that standard deviation normalization (solid) results in smaller error in residuals and larger SNRs than maximum amplitude normalization (dashed) for each AC stack of a given number of stations. (For interpretation of the references to colour in this figure legend, the reader is referred to the web version of this article.)

of EGFs in each array, we estimate the standard deviation of the residual ranges from 0.3 to 1.8 s, with an average of 0.8 s (Table 1). To see whether the residuals can be interpreted by equatorial anisotropy of the IIC model (Wang et al., 2015), we also assume seismic anisotropy of the inner core is dominated by the model of cylindrical symmetry and the P-wave velocity perturbation can be expressed as (*e.g.*, Song 1997):

$$\frac{\delta Vp}{Vp} = \alpha + \varepsilon \cos^2 \xi + \gamma \sin^2 2\xi$$

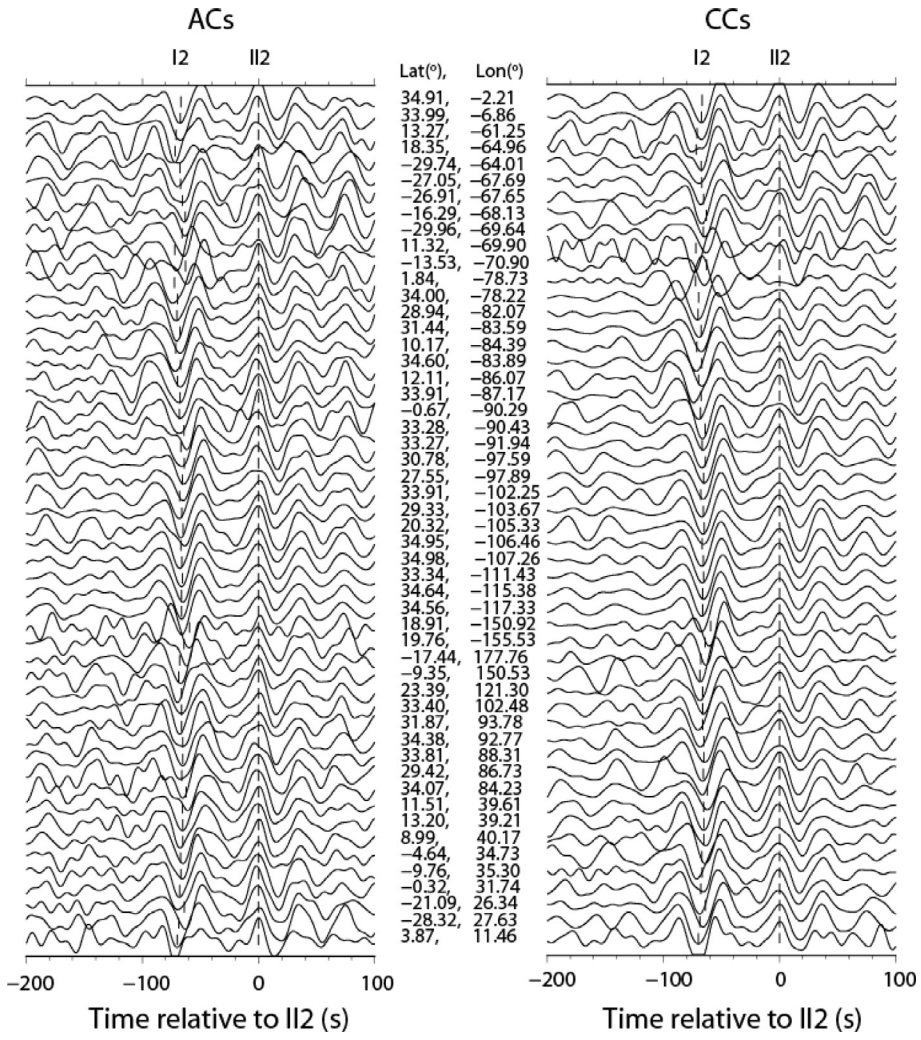

Fig. 6. Waveforms of stack ACs and CCs (latitude $\leq \pm 35°$) aligned with the II2. The arrivals of the I2 and II2 are marked by short vertical lines. (For interpretation of the references to colour in this figure legend, the reader is referred to the web version of this article.)

where ξ is the ray angle from the symmetry axis: ξ_p and ξ_e represent the ray angle from the fast axis of the OIC (spin axis) and the IIC (latitude: 9°, longitude: −89°), respectively. The anisotropy coefficients of the IIC model are $\varepsilon = 1.71\%$ and $\gamma = -1.95\%$ (Wang et al., 2015). After correcting for the OIC (Sun and Song, 2008; Wang et al., 2015), we further calculated the average residuals with the bin size of 15° based on their IIC ray angles (ξ_e). The corrections are negligible (<0.5 s in Fig. 8a) since all residuals are from low latitudes ($55° \leq \xi_p \leq 90°$). Fig. 8a shows the average residuals match the IIC model very well, with the variance reduction of 88.7%.

To compare observed data with the GD0, we calculated bi-cubic interpolation of the residuals and showed the contours (Fig. 9). Although some details are different, the main feature of the GD0 and the residuals at low latitudes is consistent with the prediction of the OIC+IIC model (Fig. 9). In general, positive residuals are observed in Central America and its antipode (Southeast Asia), which correspond to the fast axis of the IIC. While negative residuals in Hawaii, South America, East Africa are caused by the minimum P velocity at a mediate angle ξ_e (~51°). Therefore, two open rings with slow velocity are shown in both global and low-latitude data, as predicted by the OIC + IIC model (Fig. 9). The gaps of two rings can be interpreted by the slight tilt of the IIC fast axis. Compared with the prediction, asymmetry of the observed rings may result from lack of data from stations in east Australia and its antipode in Atlantic ocean. Moreover, the overall pattern of the open rings is inconsistent with a local heterogeneity beneath Central America or the Southeast Asia. Finally, high velocity beneath west Africa and near the east coast of the U.S. may reflect an asymmetric quasi-hemispherical structure of the OIC (Huang et al., 2015), though the boundary of quasi-hemispheres is still under debate (Tanaka and Hamaguchi, 1997; Creager, 1999; Niu and Wen, 2001; Garcia, 2002; Irving and Deuss, 2011; Lythgoe et al., 2014).

4. Discussion

4.1. The influence of Fresnel zone

Our claim of the IIC equatorial anisotropy was based on ray theory and the reference phase II2 was assumed to only propagate through the topmost isotropic layer of the inner core, although a finite frequency effect was considered to some extent (Wang et al., 2015). The large Fresnel zone at low frequencies may cause the II2 sampling the anisotropic region of the OIC (Fig. 2). To assess the influence, we simply estimated the Fresnel zone for both I2 and II2 from source S to the antipode S' and back to S by (Kvasnicka and Jansky, 1999):

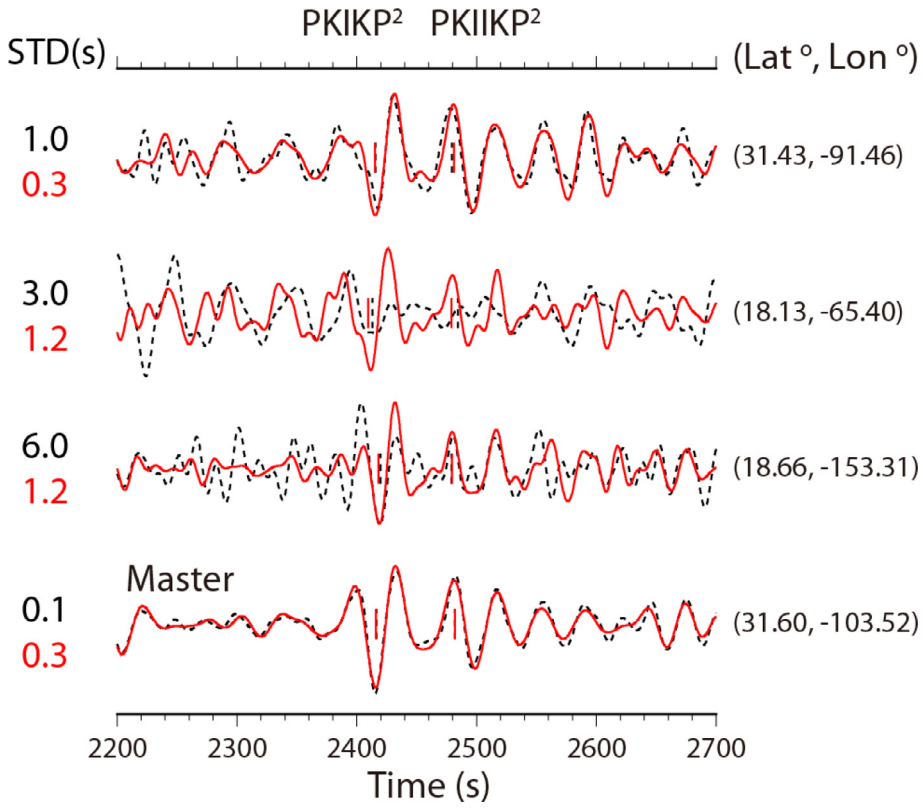

Fig. 7. Comparison of stack ACs (dotted lines) and CCs (red lines) for the master and three other arrays. Instead of ACs, the CCs from the three arrays are used because of higher stability and better SNRs. The bootstrap estimates of standard deviations of the residuals (numbers in the left: black for ACs and red for CCs) are shown. (For interpretation of the references to colour in this figure legend, the reader is referred to the web version of this article.)

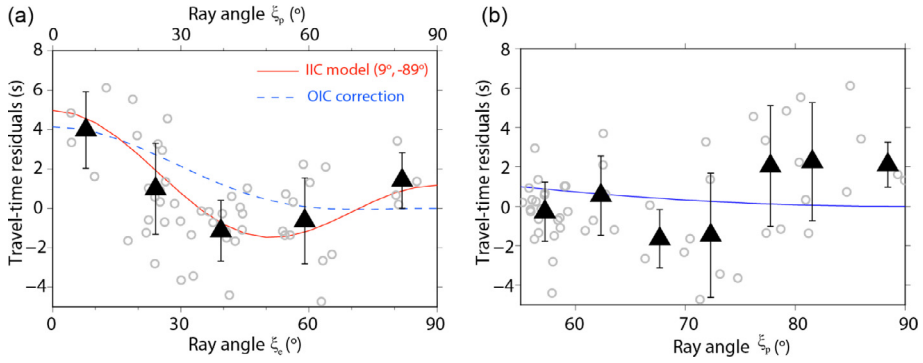

Fig. 8. Comparisons of corrected residuals (open circles) aligned with different symmetry (fast) axes. (a) Corrected residuals versus the ray angle ξ_e (bottom horizontal axis) from the fast axis of the IIC (9°, −89°). The red solid line is the prediction for the IIC model (Wang et al., 2015). The blue dashed line is the correction versus ray angle ξ_p (upper horizontal axis) from the spin axis based on the average OIC model (Sun and Song, 2008). (b) Corrected residuals versus the ray angle ξ_p (horizontal axis) from the spin axis. The solid blue line is the prediction of the best-fitting model ($\varepsilon = 0.018$, $\gamma = -0.0016$) from Romanowicz et al. (2016). Triangle and error bar are the mean and the ± one standard deviation over about 15° (a) or 5° (b) ray angle interval.

$$2 * |t_{SF} + t_{SrF} - t_{SSr}| \leq T/2$$

where t is the travel time of the ray between two points and T is the period of the impulse. Multiplying by 2 is due to the round-trip for the I2 and II2. Point F is in the Fresnel zone if above condition is satisfied.

Fig. 2 shows the sensitive region of the I2 could be up to ~700 km from the center of the core. This volume is larger than the assumed radius of the IIC (~600 km). Thus, arrival time of the I2 is affected by anisotropic structure of both IIC and OIC when the ray passes through the IIC. However, considering narrow range of the ξ_p ($\geq 55°$ and $\leq 90°$), the influence of the OIC is negligible (<0.5 s in Fig. 8) because the velocity variation as a function of the ray angle from the OIC anisotropy is small for the equatorial paths of the low-latitude stations.

On the other hand, Fresnel volume of the II2 (T = 40 s) can be ~200 km below the inner core boundary, deeper than the isotropic layer (~100 km) at the topmost inner core. As a result, the anisotropy of the OIC can affect the reference phase II2. The difference of ray angle (ξ_p) between the I2 and the II2 at its turning point, is about 20°. Based on cylindrically symmetric model of the OIC, we estimated the maximum variation of the II2 by:

$$2 * T_0 * ((\alpha + \varepsilon \cos^2(70 + \theta) + \gamma \sin^2 2(70 + \theta)) + (\alpha + \varepsilon \cos^2(70 - \theta) + \gamma \sin^2 2(70 - \theta)))/2$$

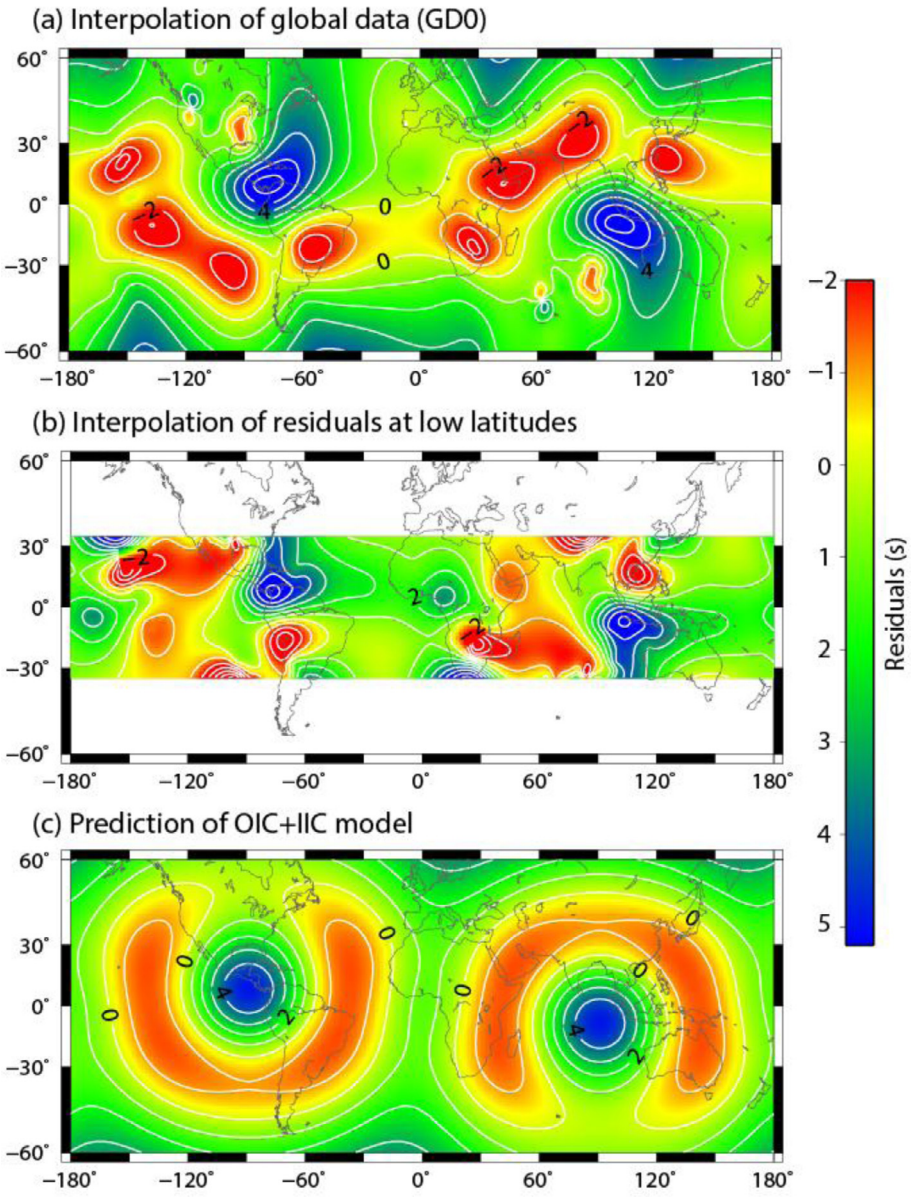

Fig. 9. Interpolation of observed residuals for global (a), low-latitude (b) data and the prediction (c) with the combination of the OIC and IIC model. The contours of the residuals are plotted (white lines).

where T_0 is travel time of phase PKIIKP propagating in the inner core (~150 s). θ is the latitude of the station. When the station is on the equator, ray angle ξ_p of the II2 at its turning point is ~70°. We calculated two legs of the PKIIKP and then double it due to the round-trip for the II2. The maximum influence for the II2 is less than 1.1 s at low latitudes (within ±35°) based on the OIC model (ε = 1.862%, γ = −0.583%) proposed by Sun and Song (2008). Taking account of the isotopic layer (~100 km) at the topmost inner core, the influence of the II2 due to large Fresnel zone, would be insignificant (<1.1 s), compared with the variation of observed residuals (σ = 2.4 s).

4.2. Comparison with study using earthquake-based absolute travel times

Recently, Romanowicz et al. (2016) argued that the model of the equatorial IIC does not fit earthquake-based travel times of the phase PKIKP at near-antipodal distances (165°–180°). They questioned "whether the paths corresponding to the autocorrelation functions actually correspond to the assumed ballistic paths between station and antipode and/or whether they have been properly computed with anisotropic ray tracing, which is particularly important for the reference phase PKIIKP". We address the issue below.

Significant evidence suggests that the retrieved I2 and II2 phases from seismic interferometry (especially the ACs) are real and can be used to constrain the structure of the inner core. In theory, it has been demonstrated the cross-correlation of two recordings, from diffuse wavefields (Lobkis and Weaver, 2001; Campillo and Paul, 2003) or uncorrelated noise sources (Wapenaar and Fokkema, 2006), can reconstruct the EGFs between two receivers. For the phases passing through the inner core, the I2 was observed by stacking cross correlations between USArray stations (Lin et al., 2013). At large distances (145° ~ 180°), triplicated PKP phases (PKIKP, PKPab and PKPbc) were extracted from noise correlations between the arrays in South America and China Regional Seismic

Networks (Xia et al., 2016). By simulating coda interferometry process (inputting synthetics of earthquake coda to obtain CCs), the stacked I2 (Boue et al., 2014) and II2 (Wu et al., 2016; Huang et al., 2016) were re-constructed. It is worth noting that arrival times and slownesses of core phases from above correlation studies are consistent with theoretical calculations. The polarities of the observed I2 and II2 are also in accordance with the synthetics (see Fig. S6 in Wang et al., 2015). Furthermore, the waveforms of both phases from coda auto-correlation are similar as the cross-correlations (Fig. 6 and see Fig. S2a in Wang et al., 2015) at small distances. Meanwhile, stacked AC may avoid the lack of energy equipartition of the coda and provide more accurate residuals (Sens-Schonfelder et al., 2015). In general, the global dataset (GD0) reflects a decreasing trend of the velocity with the increasing angle ξ_p from the spin axis, consistent with the polar anisotropy in the OIC. The noise-based residuals are compatible with earthquake-based PKIIKP-PKIKP study (Niu and Chen, 2008) at near-antipodal distances (Wang et al., 2015). These evidences confirm both phases (the I2 and II2) can be retrieved by seismic interferometry and their travel times can be used to study the IIC.

There are a number of challenges in constraining the equatorial anisotropy (if true) of the IIC using earthquake-based PKIKP arrival-time data. First, source uncertainties and the heterogeneity in the crust and mantle can significantly affect travel-time of the PKIKP and hence may bias the inference of the structure of the inner core. For instance, 10 km mislocation in depth for an earthquake leads to ~1.8 s error of PKIKP travel time. Romanowicz et al. (2016) used relocated EHB catalog (Engdahl et al., 1998) for older events and the ISC catalog for more recent events. They corrected the PKIKP arrival times for different tomographic models. They found the best-fitting fast axis points to the N-S direction with large variance reductions (at least 80%). But, in their calculations (Table 1 of Romanowicz et al., 2016), the largest and smallest variance reduction are corresponding to no mantle correction (93%) and the most recent model (80.2% for the SEMUCB model in French and Romanowicz, 2014), respectively. This, to some extent, indicates the corrections of tomographic models are incompatible with the model of the inner core. We should expect improvements of the PKIKP data corrected for the mantle to fit the model of the inner core, if the N-S fast axis is true or if the mantle corrections are adequate.

Second, limited sampling from earthquake-based PKIKP data poses a significant challenge. To sample the IIC, near-antipodal distance is required for traditional PKIKP studies. But antipodal data are severely limited by spatial distribution of earthquakes and ~70% oceanic coverage of Earth. The IIC model by Wang et al. (2015) predicts travel time variation of about 7.0 s (between fast axis and slow intermediate angle) for I2 or about 3.5 s for the single-trip PKIKP at antipodal distance. The prediction for PKIKP is about 3.4 s at distance of 176°. However, the travel time prediction by Romanowicz et al. (2016) (the green line in their Fig. 2f) for the same model (Wang et al. 2015) for the PKIKP in the IIC varies only within 1 s, which seems an error in the calculation. The averages of the observations (in Fig. 2f of Romanowicz et al., 2016) do show a larger variation of up to 3 s between the small ξ_e angles and the intermediate angles; the amplitude and the trend seem close what the IIC model of Wang et al. would predict. However, the complex pattern in the data in Fig. 2e of Romanowicz et al. (2016) cannot be fit by any simple axisymmetric anisotropy model, although the data at the smaller distances are less affected by the IIC. If we align our measurements (residuals corrected for the OIC) with the N-S axis and compare with the polar anisotropy model of the IIC from Romanowicz et al. (2016) (ε=0.018, γ=-0.0016) (Fig. 8b), the model prediction actually shows the opposite trend to the data. Correcting for the model by Romanowicz et al. (2016), the data would increase the variance by 21.4%. This compares with the variance reduction of 88.7% for the equatorial anisotropy model of the IIC by Wang et al. (2015) (Fig. 8a) (see above).

The third challenge is the relatively large error in picking arrival times (even by hand), compared with waveform correlation techniques.

In summary, because of the large uncertainties of using the ballistic arrival-time data in Romanowicz et al. (2016) to constrain the IIC anisotropy, we are not convinced that the IIC model of Wang et al. (2015) is not compatible with the earthquake-based travel time data. The issue needs to be explored furthermore using both noise interferometry and ballistic waves (arrival times or preferably differential travel times).

4.3. Possible mechanisms for the equatorial anisotropy

The change of near-equatorial anisotropy in the IIC to the N-S anisotropy in the OIC obviously calls for an explanation of the physical mechanism. The inner core anisotropy arises from the preferred alignment of anisotropic iron crystals (Brown and McQueen, 1986; Stixrude and Cohen,1995; Song, 1997). Many proposals for the N-S anisotropy have been made, including two general categories: (1) alignment established during solidification (Bergman, 1997); (2) alignment arising from solid-state convective flow in the inner core (Jeanloz and Wenk, 1988; Yoshida et al., 1996; Karato, 1999), which may be driven by differential growth of the inner core (Yoshida et al., 1996) or the Maxwell stress from the magnetic field generated in the outer core (Karato, 1999). To explain the N-S anisotropy, symmetry around the Earth's rotation axis needs to be invoked. As the rotation axis of the inner core is thought to be stable, it seems difficult to use the same mechanisms for the equatorial anisotropy of the IIC.

However, one may still speculate possible mechanisms. (1) Change of tectonic regime over the history of the inner core. Numerical simulations suggest that the deformation involves the whole inner core at the earlier stage to a regime in which it is confined to the upper part only at the later stage (Deguen and Cardin, 2011). Thus the inner part can be understood as a fossil anisotropy separated from the outer part.

(2) A proto-inner core (Helffrich and Brasser, 2015). At the very earliest stage of Earth's accretion, their simulation indicates that a proto-inner core may develop due to low enough temperatures at the center of our planet. After the differentiation process during or after the end of accretion, the composition of the OIC is different from the relic (the IIC) at the earliest stage, which can explain the shift of fast axis and different form of the anisotropy.

(3) Change of dominant geomagnetic field. Currently the geomagnetic field is dominated by a N-S dipole and the Geocentric Axial Dipole (GAD) hypothesis states that the paleomagnetic field dipole component is in a long-time (e.g. ~10,000 years) average aligned with the rotation axis (Hospers, 1954), which is the basis for paleotectonic reconstructions. However, an equatorial geomagnetic dipole was suggested during the Ediacaran (around 600 Ma) (Abrajevitch and Van der Voo, 2010). As the dominant orientation of the dipole shifts, the corresponding Maxwell stress may result in the change of fast axis between the IIC and the OIC.

5. Conclusion

The calculation of the Fresnel zone at low frequencies (T = ~40 s) showed the I2 in the IIC part and the II2 could be affected by the anisotropic structure of the OIC. To reduce possible contaminations from large Fresnel zone and to reduce the influence of N-S anisotropy in the OIC, we retrieved EGFs of both phases from stations at low latitudes (within ±35°) using both ACs and CCs of earthquake coda. The estimated influence of the Fresnel zone is

insignificant (<1.1 s), in contrast to the variation (~10.9 s) and standard deviation (~2.4 s) of low-latitude residuals.

Compared with our previous global study (Wang et al., 2015), some improvement strategies were applied to extract more accurate and stable EGFs. We used a longer coda duration (10,000–40,000 s instead of 10,000–30,000 s) after large earthquakes (all types with magnitude ≥7.0 earthquakes) and a longer time span (1990–2013 instead of 2005–2012). The automatic grouping method, the standard-deviation normalization, and the selection filter help improve SNRs and obtain more robust EFGs. The systematic examination of CCs, in addition to ACs, also allowed us to pick up a few more high-quality EGFs. The quality of our total EGFs from 52 arrays (including 49 ACs and 3 CCs) allowed us to measure the relative times using automatic waveform cross correlation.

The low-latitude residuals match very well previous IIC model with a quasi-equatorial fast axis (Wang et al., 2015). It is difficult to explain large variation (up to ~10.9 s) near the equator by a model with the N-S fast axis. The bi-cubic interpolation of the residuals also shows a similar pattern with previous global dataset, including the fast axis and two low-velocity open rings. Therefore, our results further support the equatorial anisotropy in the IIC with the fast axis near Central America and the Southeast Asia. Speculations for the shift of the fast axis between the OIC and the IIC include: change of deformation regimes during the inner core history, change of geomagnetic field, and a proto-inner core.

Acknowledgement

All data were obtained from the IRIS DMC. Figures were plotted using the GMT software (Wessel and Smith, 1991). We thank constructive reviews from Vernon Cormier and an anonymous reviewer. This work was supported by the National Natural Science Foundation of China (41404037, 41330209) and the US National Science Foundation (EAR 1620595).

References

Abrajevitch, A., Van der Voo, R., 2010. Incompatible Ediacaran paleomagnetic directions suggest an equatorial geomagnetic dipole hypothesis. Earth Planet. Sci. Lett. 293 (1), 164–170.
Alboussiere, T., Deguen, R., Melzani, M., 2010. Melting-induced stratification above the Earth's inner core due to convective translation. Nature 466 (7307), 744–747.
Beghein, C., Trampert, J., 2003. Robust normal mode constraints on inner-core anisotropy from model space search. Science 299, 552–555.
Bensen, G.D., Ritzwoller, M.H., Barmin, M.P., Levshin, A.L., Lin, F., Moschetti, M.P., Shapiro, N.M., Yang, Y., 2007. Processing seismic ambient noise data to obtain reliable broad-band surface wave dispersion measurements. Geophys. J. Int. 169, 1239–1260.
Bergman, M.I., 1997. Measurements of electric anisotropy due to solidification texturing and the implications for the Earth's inner core. Nature 389, 60–63.
Boue, P., Poli, P., Campillo, M., Pedersen, H., Briand, X., Roux, P., 2013. Teleseismic correlations of ambient seismic noise for deep global imaging of the Earth. Geophys. J. Int. 194, 844–848.
Boue, P., Poli, P., Campillo, M., Roux, P., 2014. Reverberations, coda waves and ambient noise: Correlations at the global scale and retrieval of the deep phases. Earth Planet. Sc. Lett. 391, 137–145.
Brëger, L., Tkalčić, H., Romanowicz, B., 2000. The effect of D″on PKP (AB− DF) travel time residuals and possible implications for inner core structure. Earth Planet. Sci. Lett. 175 (1), 133–143.
Brown, J.M., Mcqueen, R.G., 1986. Phase-transitions, Gruneisen-parameter, and elasticity for shocked iron between 77-Gpa and 400-Gpa. J. Geophys. Res.-Sol. Ea. 91 (B7), 7485–7494.
Campillo, M., Paul, A., 2003. Long-range correlations in the diffuse seismic coda. Science 299, 547–549.
Cao, A., Romanowicz, B., 2007. Test of the innermost inner core models using broadband PKIKP travel time residuals. Geophys. Res. Lett. 34, L08303. http://dx.doi.org/10.1029/2007GL029384.
Cormier, V.F., Stroujkova, A., 2005. Waveform search for the innermost inner core. Earth Planet. Sci. Lett. 236, 96–105.
Cottaar, S., Buffett, B., 2012. Convection in the Earth's inner core. Phys. Earth Planet. Int. 198, 67–78.
Creager, K.C., 1992. Anisotropy of the inner core from differential travel-times of the phases PKP and PKIKP. Nature 356, 309–314.
Creager, K.C., 1999. Large-scale variations in inner core anisotropy. J. Geophys. Res.-Sol. Ea. 104, 23127–23139.
Deguen, R., Cardin, P., 2009. Tectonic history of the Earth's inner core preserved in its seismic structure. Nat. Geosci. 2, 418–421.
Deguen, R., Cardin, P., 2011. Thermochemical convection in Earth's inner core. Geophys. J. Int. 187, 1101–1118.
Engdahl, E.R., van der Hilst, R., Buland, R., 1998. Global teleseismic earthquake relocation with improved travel times and procedures for depth determination. Bull. Seism. Soc. Am. 88, 722–743.
French, S., Romanowicz, B., 2014. Whole-mantle radially anisotropic shear velocity structure from spectral-element waveform tomography. Geophys. J. Int. 199, 1303–1327.
Garcia, R., 2002. Constraints on upper inner-core structure from waveform inversion of core phases. Geophys. J. Int. 150, 651–664.
Helffrich, G.R., Brasser, R., 2015, Age and Formation Mechanism for an Innermost Inner Core. Abstract presented at 2016, Fall Meeting, AGU.
Hospers, J., 1954. Rock magnetism and polar wandering. Nature 173, 1183–1184.
Huang, H.H., Lin, F.C., Tsai, V.C., Koper, K.D., 2015. High-resolution probing of inner core structure with seismic interferometry. Geophys. Res. Lett. 42, 10622–10630.
Huang, H.H., Tsai, V.C., Lin, F.C., Wang, W.T., Chaput, J.A., 2016, Synthesis of body-wave information from global earthquake coda correlation: A numerical evaluation. Abstract presented at 2016, Fall Meeting, AGU.
Irving, J.C.E., Deuss, A., 2011. Hemispherical structure in inner core velocity anisotropy. J. Geophys. Res.-Sol. Ea. 116, B04307. http://dx.doi.org/10.1029/2010JB007942.
Ishii, M., Dziewonski, A.M., 2002. The innermost inner core of the earth: Evidence for a change in anisotropic behavior at the radius of about 300 km. Proc. Nat. Acad. Sci. U.S.A. 99, 14026–14030.
Ishii, M., Tromp, J., Dziewonski, A.M., Ekstrom, G., 2002. Joint inversion of normal mode and body wave data for inner core anisotropy – 1. Laterally homogeneous anisotropy. J. Geophys. Res.-Sol. Ea. 107 (B12), 2379. http://dx.doi.org/10.1029/2001JB000712.
Jeanloz, R., Wenk, H.R., 1988. Convection and Anisotropy of the Inner Core. Geophys. Res. Lett. 15 (1), 72–75.
Karato, S., 1999. Seismic anisotropy of the Earth's inner core resulting from flow induced by Maxwell stresses. Nature 402, 871–873.
Kvasnicka, M., Jansky, J., 1999. Fresnel volumes corresponding to PKP waves in the IASP91 model. J. Seismol. 3 (4), 375–391.
Labrosse, S., Macouin, M., 2003. The inner core and the geodynamo. C.R. Geosci. 335, 37–50.
Li, X., Cormier, V.F., 2002. Frequency-dependent seismic attenuation in the inner core, 1. A viscoelastic interpretation. J. Geophys. Res.-Sol. Ea. 107 (B12), 2361. http://dx.doi.org/10.1029/2002JB001795.
Liang, C., Song, X., Huang, J., 2004. Tomographic inversion of Pn travel times in China. J. Geophys. Res.-Sol. Ea. 109, B11304. http://dx.doi.org/10.1029/2003JB002789.
Lin, F.C., Tsai, V.C., 2013. Seismic interferometry with antipodal station pairs. Geophys. Res. Lett. 40, 4609–4613.
Lin, F.C., Tsai, V.C., Schmandt, B., Duputel, Z., Zhan, Z.W., 2013. Extracting seismic core phases with array interferometry. Geophys. Res. Lett. 40, 1049–1053.
Lobkis, O.I., Weaver, R.L., 2001. On the emergence of the Green's function in the correlations of a diffuse field. J. Acoust. Soc. Am. 110, 3011–3017.
Lythgoe, K.H., Deuss, A., Rudge, J.F., Neufeld, J.A., 2014. Earth's inner core: innermost inner core or hemispherical variations? Earth Planet. Sci. Lett. 385, 181–189.
Morelli, A., Dziewonski, A.M., Woodhouse, J.H., 1986. Anisotropy of the inner core inferred from PKIKP travel times. Geophys. Res. Lett. 13, 1545–1548.
Nishida, K., 2013. Global propagation of body waves revealed by cross-correlation analysis of seismic hum. Geophys. Res. Lett. 40, 1691–1696.
Nakata, N., Chang, J.P., Lawrence, J.F., Boue, P., 2015. Body wave extraction and tomography at Long Beach, California, with ambient-noise interferometry. J. Geophys. Res.-Sol. Ea. 120, 1159–1173.
Niu, F.L., Chen, Q.F., 2008. Seismic evidence for distinct anisotropy in the innermost inner core. Nat. Geosci. 1, 692–696.
Niu, F.L., Wen, L.X., 2001. Hemispherical variations in seismic velocity at the top of the Earth's inner core. Nature 410, 1081–1084.
Poli, P., Campillo, M., Pedersen, H., Grp, L.W., 2012. Body-wave imaging of earth's mantle discontinuities from ambient seismic noise. Science 338, 1063–1065.
Romanowicz, B., Cao, A., Godwal, B., Wenk, R., Ventosa, S., Jeanloz, R., 2016. Seismic anisotropy in the Earth's innermost inner core: Testing structural models against mineral physics predictions. Geophys. Res. Lett. 43, 93–100.
Shearer, P.M., 1994. Constraints on inner-core anisotropy from PKP(DF) travel-times. J. Geophys. Res.-Sol. Ea. 99, 19647–19659.
Sens-Schonfelder, C., Snieder, R., Stahler, S.C., 2015. The lack of equipartitioning in global body wave coda. Geophys. Res. Lett. 42, 7483–7489.
Shapiro, N.M., Campillo, M., Stehly, L., Ritzwoller, M.H., 2005. High-resolution surface-wave tomography from ambient seismic noise. Science 307, 1615–1618.
Song, X.D., 1997. Anisotropy of the earth's inner core. Rev. Geophys. 35, 297–313.
Song, X.D., Helmberger, D.V., 1995a. Depth Dependence of Anisotropy of Earths Inner-Core. J. Geophys. Res.-Sol. Ea. 100, 9805–9816.
Song, X.D., Helmberger, D.V., 1995b. A P wave velocity model of Earth's core. Geophys. Res.-Sol. Ea. 100 (B6), 9817–9830.
Song, X.D., Helmberger, D.V., 1997. PKP differential travel times: Implications for 3-D lower mantle structure. Geophys. Res. Lett. 24 (15), 1863–1866.
Song, X.D., Richards, P.G., 1996. Seismological evidence for differential rotation of the Earth's inner core. Nature 382, 221–224.

Stixrude, L., Cohen, R.E., 1995. High-pressure elasticity of iron and anisotropy of earth's inner-core. Science 267 (5206), 1972–1975.
Sun, X.L., Song, X.D., 2008. Tomographic inversion for three-dimensional anisotropy of Earth's inner core. Phys. Earth Planet. Int. 167, 53–70.
Tanaka, S., Hamaguchi, H., 1997. Degree one heterogeneity and hemispherical variation of anisotropy in the inner core from PKP(BC)-PKP(DF) times. J. Geophys. Res.-Sol. Ea. 102, 2925–2938.
Tromp, J., 1993. Support for anisotropy of the earths inner-core from free oscillations. Nature 366, 678–681.
Wang, T., Song, X., Xia, H.H., 2015. Equatorial anisotropy in the inner part of Earth's inner core from autocorrelation of earthquake coda. Nat. Geosci. 8, 224–227.
Wapenaar, K., Fokkema, J., 2006. Green's function representations for seismic interferometry. Geophysics 71. http://dx.doi.org/10.1190/1.2213955.
Wessel, P., Smith, W.H., 1991. Free software helps map and display data, EOS. Trans. Am. Geophys. Union 72 (41), 441–446.
Woodhouse, J.H., Giardini, D., Li, X.D., 1986. Evidence for inner core anisotropy from free oscillations. Geophys. Res. Lett. 13, 1549–1552.
Wu, B.J., Wang, T., Xia, H.H., 2016. Core Phases Retrieval from Cross-Correlations of Synthetic Seismic Coda. Abstract presented at 2016, Fall Meeting, AGU.
Xia, H.H., Song, X., Wang, T., 2016. Extraction of triplicated PKP phases from noise correlations. Geophys. J. Int. 205, 499–508.
Yao, H.J., van der Hilst, R.D., 2009. Analysis of ambient noise energy distribution and phase velocity bias in ambient noise tomography, with application to SE Tibet. Geophys. J. Int. 179, 1113–1132.
Yoshida, S., Sumita, I., Kumazawa, M., 1996. Growth model of the inner core coupled with the outer core dynamics and the resulting elastic anisotropy. J. Geophys. Res.-Sol. Ea. 101, 28085–28103.
Zheng, S.H., Sun, X.L., Song, X.D., Yang, Y.J., Ritzwoller, M.H., 2008. Surface wave tomography of China from ambient seismic noise correlation. Geochem. Geophys. Geosyst. 9, Q05020. http://dx.doi.org/10.1029/2008GC001981.